RSC Advances

PAPER

View Article Online
View Journal | View Issue

Cite this: *RSC Adv.*, 2019, **9**, 4106

Fullerene derivative induced morphology of bulk heterojunction blends: PIPCP:$PC_{61}BM$†

Tzu-Yen Huang,[a] Hongping Yan,[ab] Maged Abdelsamie,[a] Victoria Savikhin,[ac] Sebastian A. Schneider,[ad] Niva A. Ran,[e] Thuc-Quyen Nguyen,[e] Guillermo C. Bazan[e] and Michael F. Toney*[a]

Received 21st December 2018
Accepted 18th January 2019

DOI: 10.1039/c8ra10488c

rsc.li/rsc-advances

The performance of organic solar cells (OSCs) depends crucially on the morphology in bulk heterojunctions (BHJs), including the degree of crystallinity of the polymer and the amount of each material phase: aggregated donor, aggregated acceptor, and molecular mixed donor : acceptor phase. In this paper, we report the BHJ morphology of as-cast blend films incorporating the polymer PIPCP as the donor and [6,6]-phenyl-C_{61}-butyric acid methyl ester ($PC_{61}BM$) as the acceptor. Tracking the scattering intensity of $PC_{61}BM$ as a function of $PC_{61}BM$ concentration shows that $PC_{61}BM$ aggregates into donor-rich domains and there is little to no phase where the $PC_{61}BM$ and PIPCP are intimately mixed. We further find that on blending the scattering peak due to PIPCP ordering along the backbone increases with decreasing PIPCP fraction, which is attributed to improved ordering of PIPCP due to the presence of $PC_{61}BM$. Our results suggest that the improved ordering of PIPCP along the backbone (consistent with an increased conjugation length) with blending contributes to the observed low open-circuit voltage energy loss.

1. Introduction

Solution-processed organic solar cells (OSCs) are attractive as inexpensive renewable energy harvesting materials because of their low manufacturing costs, roll-to-roll processing, and flexible large-area devices.[1–4] Steady progress in the development of conjugated polymers with donor/acceptor structures has resulted in power conversion efficiencies (PCEs) reaching greater than 13% for single cells and up to 17% for tandem cells[5,6] based on the bulk heterojunction (BHJ) architecture. The BHJ is a blend of donor and acceptor semiconductors with partial phase separation and provides large interfacial area for charge separation. The phase-separated morphology consists of relatively pure donor and acceptor domains, and a molecularly mixed donor : acceptor region (*i.e.*, the mixed phase). The donor- and acceptor-rich phases in the film form an interpenetrating network to transport charge carriers after exciton dissociation; however, in addition to the pure phase, the interface between the donor and the acceptor phase may not be molecularly sharp, but gradual. This molecular mixed phase in the BHJ film is still not fully understood, although there is some evidence that the mixed phase enhances generation of charge carriers.[7] To date, the relative amounts of pure and mixed phase only have been reported for some polymer : fullerene systems[8,9] and mixed phases demonstrated for certain well-known polymers such as poly(3-hexylthiophene-2,5-diyl) (P3HT), poly[(4,8-bis-(2-ethylhexyloxy)-benzo(1,2-*b*:4,5-*b*′)dithiophene-2,6-diyl-*alt*-(4-(2-ethylhexyl)-3-fluorothieno[3,4-*b*]thiophene-)-2-carboxylate-2-6-diyl)] (PTB7), and poly(di(2-ethylhexyloxy)benzo[1,2-*b*:4,5-*b*′]dithiophene-*co*-octylthieno[3,4-*c*]pyrrole-4,6-dione) (PBDTTPD).[10–13] In the case of the PBDTTPD polymer, X-ray scattering was utilized to quantify the mixed phase by varying the fullerene concentration in BHJs and determining the $PC_{61}BM$ diffraction. No $PC_{61}BM$ scattering was observed until the content of fullerene reached 20 wt%; therefore, Bartelt *et al.* concluded that ~20 wt% of fullerene is intimately mixed with PBDTTPD.[12] On the other hand, no mixed phase was observed in the high-performing small molecule X2 : PCBM blend in,[14,15] using a similar method.

While PIPCP:$PC_{61}BM$ BHJ blends exhibit a PCE of 6.4%, they are relevant in the context of their high open-circuit voltage (V_{OC}) of 0.86 V.[16] Ran *et al.* studied the energy loss ($E_{loss} = E_g - eV_{OC}$, where E_g is the optical bandgap) for a series of polymer donors with PCE > 5%. Compared with most polymer BHJs, PIPCP:$PC_{61}BM$ blends exhibit an exceptionally low energy loss of $E_{loss} = 0.52$ eV, while most fullerene-based BHJs have $E_{loss} > 0.6$ eV.[17,18] Furthermore, the absorption edge of PIPCP is redshifted after blending with $PC_{61}BM$ and the Urbach energy of the neat PIPCP and the blend are both small at ~27 meV.

[a]*Stanford Synchrotron Radiation Lightsource, SLAC National Accelerator Laboratory, Menlo Park, CA, USA. E-mail: mftoney@slac.stanford.edu*
[b]*Department of Chemical Engineering, Stanford University, Stanford, CA, USA*
[c]*Department of Electrical Engineering, Stanford University, Stanford, CA, USA*
[d]*Department of Chemistry, Stanford University, Menlo Park, CA, USA*
[e]*Center for Polymers and Organic Solids, Department of Chemistry and Biochemistry, University of California—Santa Barbara, Santa Barbara, CA, USA*

† Electronic supplementary information (ESI) available. See DOI: 10.1039/c8ra10488c

Transition electron microscopy (TEM) from PIPCP:PCBM blends showed well defined PIPCP lattice planes due to crystalline regions in the blends, while in the neat PIPCP such regions were not observed. These results were interpreted as showing that for the blend film, the optoelectronic behavior was due to the increase in PIPCP conjugation length with the PIPCP molecule becoming more planar.[18] PIPCP and several derivative polymers have also been investigated with grazing-incidence wide-angle X-ray scattering (GIWAXS).[19–21]

Ran *et al.* recently investigated the blend morphology of PIPCP:$PC_{61}BM$ BHJ film using resonant soft X-ray scattering (RSoXS)[17] and a number of optoelectronic measurements. They showed that the as-cast PIPCP:$PC_{61}BM$ blend film forms phase-separated donor and acceptor domains with a size of $\approx$30 nm but that annealed films were mixed and not phase separated. This was inferred to suggest that PIPCP and $PC_{61}BM$ were highly miscible, consistent with calculations of the Flory–Huggins chi parameter. Ran *et al.*[17] further comprehensively investigated the recombination and loss mechanisms and concluded that the mixed morphology caused the observed non-geminate recombination and low fill factor (FF) in devices. It is important to note here that the much less pronounced phase separation was only observed in annealed films and that the length scale of the RSoXS measurements was limited to a minimum of about 4–6 nm in diameter (set by the maximum scattering vector of 0.8 nm^{-1}). Under these conditions, the RSoXS will not resolve mixing below about 4–6 nm, corresponding to between 30 and 100 fullerenes within the volume of a pure $PC_{61}BM$ cluster. The grazing-incidence wide-angle X-ray scattering (GIWAXS) method we adopt[14,15] is, in contrast, sensitive at a smaller length scale of polymers and fullerene mixing. Thus, the accurate characterization, and thus our understanding, of donor : acceptor mixing is still limited.

In this work, we report the blend morphology of the PIPCP:$PC_{61}BM$ BHJ system with a varying ratio of components. GIWAXS is employed to investigate the BHJ morphology, using the methodology that we previously reported to elucidate the mixed phase.[15] We find that there is a negligible amount of molecularly mixed phase in as-cast PIPCP:$PC_{61}BM$ BHJs. However, the PIPCP phase may contain isolated $PC_{61}BM$ clusters that lead to high charge recombination and low FF. The presence of aggregated $PC_{61}BM$ improves the order of PIPCP polymers and surprisingly a scattering peak along the in-plane direction at q_{xy} = 0.25 $Å^{-1}$ significantly increases with increasing $PC_{61}BM$ content, showing a strengthening of the order along the backbone chain. These results provide insight into the morphology in BHJs and help developing a new class of high V_{OC} materials for OSCs.

2. Experimental

2.1 Materials

The synthesis of PIPCP, used as the donor material, has been described previously.[16] $PC_{61}BM$ was purchased from Nano-C. Chloroform (CF) and chlorobenzene (CB) were purchased from Sigma-Aldrich. The chemical structures of PIPCP and $PC_{61}BM$ are displayed in Fig. 1. All chemicals were received and used without further purification.

2.2 Preparation of PIPCP:$PC_{61}BM$ blend films

The solution of PIPCP:$PC_{61}BM$ blend was prepared in the CF : CB (3 : 2 v/v%) co-solvent. To investigate the effect of $PC_{61}BM$ concentration on the morphology, the total solids concentration of active layer solution was maintained at 20 mg ml^{-1} while varying the composition of $PC_{61}BM$ (0–100 wt%). Prior to sample preparation, the Si substrates were cleaned in detergent, DI water, acetone, and isopropyl alcohol. After routine solvent cleaning, the Si substrates were treated with UV ozone for 15 min. The active layer solution (PIPCP:$PC_{61}BM$) was spin-coated in a nitrogen glovebox (2000 rpm, 60 s) onto the Si substrate at room temperature and the films were not annealed. A Bruker Dektak XT-S Stylus profilometer (stylus force: 1–15 mg with LIS 3 sensor and scan length range: 55 mm (2 in.); 200 mm (8 in.) with scan stitching capability) was used to measure the film thickness of the active layer.

2.3 Grazing-incidence wide-angle X-ray scattering (GIWAXS) measurement

GIWAXS was measured at the Stanford Synchrotron Radiation Lightsource (SSRL) beamline 11-3 in a helium-filled chamber with an X-ray wavelength of 0.9752 Å and sample-to-detector distance of 25 cm at an incident angle of 0.12°. For the *in situ* thermal measurement, a GIWAXS image was taken initially at room temperature before any thermal treatment. The samples were then heated to the annealing temperature (50, 100, 150,

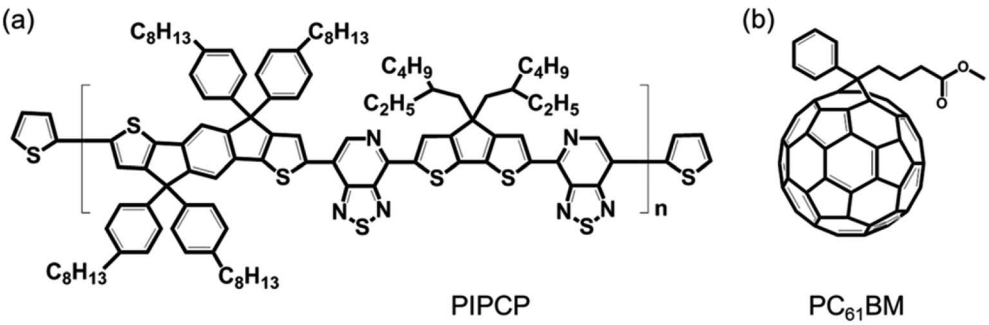

Fig. 1 The chemical structure of (a) PIPCP and (b) $PC_{61}BM$.

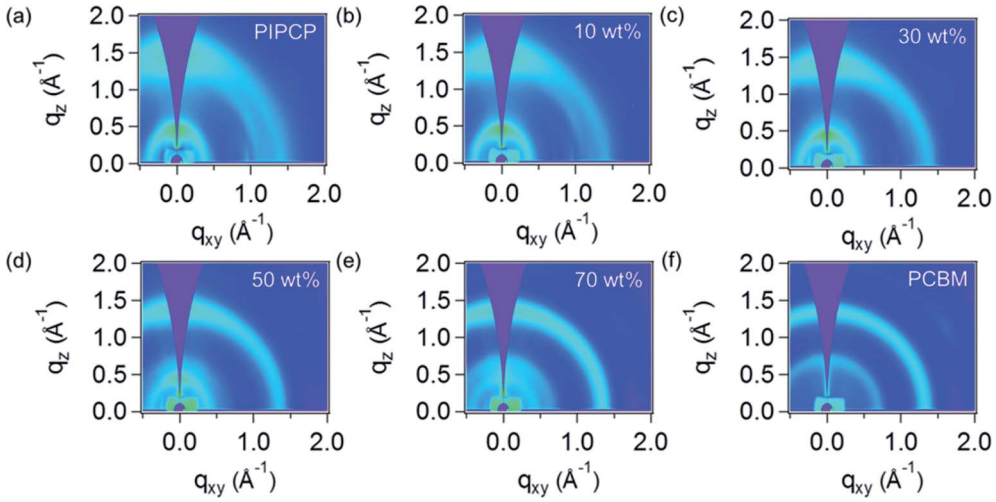

Fig. 2 The GIWAXS pattern of PIPCP:$PC_{61}BM$ BHJ blends with various blend ratio. The labeled weight percentage corresponds to the content of $PC_{61}BM$ in the active layer: (a) 0% (or neat PIPCP), (b) 10%, (c) 30%, (d) 50%, (e) 70%, and (f) 100% (or neat $PC_{61}BM$).

200 and 225 °C) and allowed to equilibrate at each temperature for 20 min before the data collection (at these elevated temperatures). The spectra were recorded on a 2D X-ray detector (MX225, Rayonix, L.L.C.) with a pixel size of 73 μm (3072 × 3072 pixels) and analyzed using the Nika and WAXStools package for Igor software (WaveMetrics, Inc.).[15,22] In this work, the polar angle (χ) is defined as the angle of the observed diffraction from the normal to the substrate, with $\chi = 0°$ defined as perpendicular to the substrate and $\chi = 90°$ parallel to the substrate. The out-of-plane sector is considered at 0–20° and an in-plane sector is 70–90°.

3. Results & discussion

Fig. 1(a) and (b) display the chemical structure of PIPCP and $PC_{61}BM$. PIPCP contains a backbone comprised of IDT-PT-CPDT-PT repeat subunits where IDT = indacenodithiophene, PT = pyridyl[2,1,3]thiadiazole and CPDT = cyclopentadithiophene.

3.1 GIWAXS of PIPCP:$PC_{61}BM$ blend films

GIWAXS was employed to quantify the mixed phase in BHJ films by tracking the $PC_{61}BM$ scattering intensity as outlined above. Fig. 2 shows the GIWAXS pattern of PIPCP:$PC_{61}BM$ BHJ blends incorporating 0, 10, 30, 50, 70 and 100 wt% of $PC_{61}BM$. The complete GIWAXS patterns incorporating the different $PC_{61}BM$ ratios are provided in Fig. s1.† The pristine PIPCP film scattering pattern has peaks from lamellar stacking at $q \approx 0.4$ Å^{-1} (≈17 Å *d*-spacing) and from π–π stacking at $q = 1.43$ Å^{-1} (4.4 Å *d*-spacing),[16] with a rather broad polar angle distribution. The scattering from π–π stacking appears generally isotropic with slight preference in the out-of-plane direction which shows some preferred face-on orientation with respect to the Si substrate. As the ratio of $PC_{61}BM$ increases to 30 and 50 wt%, the PIPCP lamellar stacking becomes more angularly isotropic and the π–π stacking begins to overlap with the scattering of $PC_{61}BM$. Further increasing $PC_{61}BM$ to more than 70 wt%, the scattering from $PC_{61}BM$ were observed at $q = 0.68$ and 1.35 Å^{-1} and the scattering peaks attributed to PIPCP become weaker.

By studying the $PC_{61}BM$ intensity as a function of $PC_{61}BM$ concentration, the behavior of $PC_{61}BM$ (aggregated *vs.* molecularly mixed with PIPCP) in the BHJ can be determined, similar to the method reported by Bartelt *et al.*[12,14,15] The intensity *vs.* scattering vector profiles (integrated over all polar angles) of PIPCP:$PC_{61}BM$ blends are summarized in Fig. 3(a). These profiles are normalized at $q = 1.0$ Å^{-1}, since scattering at this location is mostly due to diffuse background. The dependence of the $PC_{61}BM$ intensity at $q = 0.68$ Å^{-1} with concentration in this normalized plot shows that $PC_{61}BM$ contributes to the

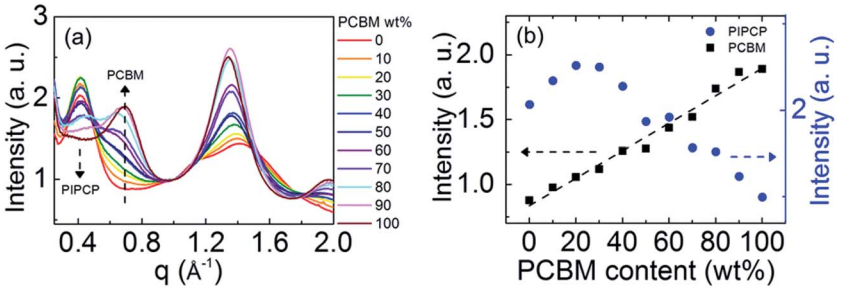

Fig. 3 (a) Polar angle integrated intensity from GIWAXS pattern of PIPCP:$PC_{61}BM$ blends varying from 0 to 100 wt% of $PC_{61}BM$. The data are normalized at $q = 1.0$ Å^{-1}. (b) The intensity of PIPCP ($q \approx 0.4$ Å^{-1}) and $PC_{61}BM$ ($q = 0.68$ Å^{-1}) scattering with different $PC_{61}BM$ content. The dashed line is a linear fit to the data.

scattering even with as little as 10% $PC_{61}BM$ content. Fig. 3(b) shows a plot of the intensity at $q = 0.68$ Å^{-1} *vs.* $PC_{61}BM$ fraction and displays a linear dependence with no onset. The $PC_{61}BM$ scattering at $q = 1.35$ Å^{-1} displays a similar tendency as shown in Fig. s2.† These observations show that $PC_{61}BM$ is aggregated even at low weight fractions and little $PC_{61}BM$ exists in an intimately mixed phase (clusters less than about 2 nm) for the PIPCP:$PC_{61}BM$ BHJ system. The low FF for PIPCP:$PC_{61}BM$ BHJs may then be due to poorly connected donor or acceptor domains and/or shallow traps that lead to severe charge recombination.

On the other hand, the scattering intensity of PIPCP at $q \approx 0.4$ Å^{-1} increases as the $PC_{61}BM$ content increases (PIPCP fraction decreases) to 20%, implying that the extent of ordering of PIPCP crystal is enhanced by the introduction of $PC_{61}BM$, then decreases with higher $PC_{61}BM$ content (>30%) in the film. This suggests that the ordering of PIPCP is improved in the presence of $PC_{61}BM$ in BHJs, consistent with TEM of PIPCP:$PC_{61}BM$ blends showing crystalline regions.[18]

Careful inspection of the GIWAXS for small q shows a scattering peak along the in plane direction at $q_{xy} = 0.25$ Å^{-1} as can be seen by the enlarged GIWAXS pattern in Fig. 4(a). (Note that the asymmetry of the X-ray window only allows observation of the left side of the image.) This corresponds to a d-spacing of ≈25 Å, close to that estimated for a monomer unit. This, together with the in-plane (q_{xy}) orientation of this peak, shows that the 0.25 Å^{-1} peak results from order along the PIPCP backbone. To gain more insight into the PIPCP morphological changes upon blending, we plot the GIWAXS in-plane line profiles of the left side of the images in Fig. 4(b). This shows how the PIPCP scattering varies on blending and remarkably illustrates that the backbone reflection at $q = 0.25$ Å^{-1} significantly increases with increasing $PC_{61}BM$ content. In addition, the lamellar stacking diffraction shifts to slightly higher q values with increasing $PC_{61}BM$ content, indicating a decrease in lamella d-spacing. To extract quantitative information of the lamella and backbone scattering, the line cuts in Fig. 4(b) are fit to a small background term (accounting for scattering from the substrate and sample cell) and three peaks due to the 0.25 Å^{-1} peak, the lamella peak and the $PC_{61}BM$ scattering, as shown in Fig. s3.†

Fig. 4(c) plots the PIPCP lamellar d-spacing and the peak full-width at half maximum (FWHM) upon increasing the $PC_{61}BM$ fraction. The d-spacing (16.8 Å) of PIPCP lamellar stacking remains constant for samples with $PC_{61}BM$ content up to 20 wt% but starts to decrease after incorporating ≥30 wt% of $PC_{61}BM$. The FWHM of the lamellar peak here provides insight into the regularity of the lamellar packing. FWHM decreases slightly on initial blending, showing that the lamellar stacking becomes somewhat more ordered. Above about 30% $PC_{61}BM$, the lamellae FWHM increases slightly with increasing $PC_{61}BM$ content. Importantly, as shown in Fig. 4(d), the backbone scattering peak intensity of PIPCP at 0.25 Å^{-1} increases significantly (more than 3×) upon increasing the $PC_{61}BM$ fraction from 0 to 30%, showing that the order along the PIPCP backbone is markedly increased. The similar tendency can be observed when the scattering intensity is normalized by the corresponding content of PIPCP (Fig. s4†). The improved backbone order of PIPCP that we observe is consistent with an increased effective conjugation length of polymer after blending of $PC_{61}BM$ and the observed red shift in the blend absorption.

3.2 Temperature dependence of PIPCP:$PC_{61}BM$ blend films

We used *in situ* GIWAXS measurements to monitor the thin film morphology evolution with thermal annealing, in order to understand any thermally induced changes and to verify our hypothesis that the $q = 0.25$ Å^{-1} peak is due to the ordering along the polymer backbone. We note that Wang *et al.* previously reported that no thermal transitions were observed for the neat PIPCP polymer up to a temperature of 280 °C.[16] The

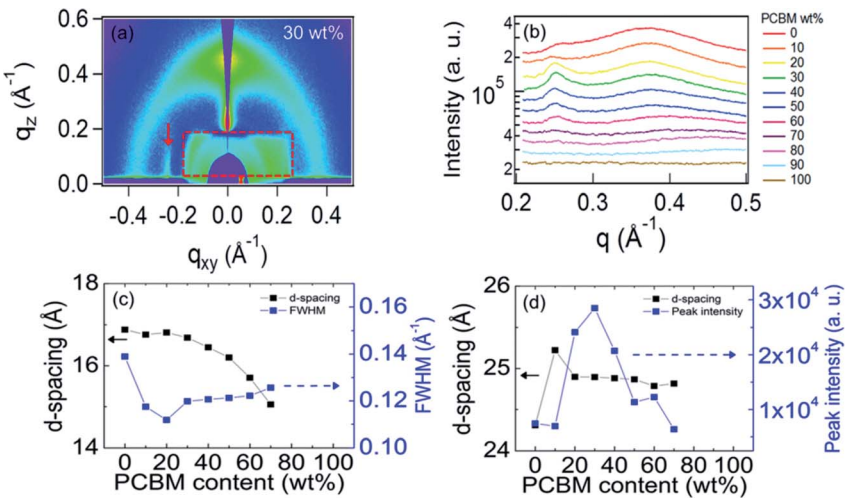

Fig. 4 (a) The enlarged GIWAXS pattern of PIPCP:$PC_{61}BM$ BHJ blends incorporating 30 wt% $PC_{61}BM$. Red rectangle (dashed line) is the X-ray window and arrow points to the backbone peak at 0.25 Å^{-1}. (b) The in-plane line profiles from the GIWAXS pattern for different PIPCP:$PC_{61}BM$ blend ratio. (c) The lamellae d-spacing and FWHM at $q \approx 0.40$ Å^{-1} with different $PC_{61}BM$ content. (d) The d-spacing along the polymer backbone and peak intensity at $q = 0.25$ Å^{-1} with different $PC_{61}BM$ content. (c and d) are taken from peak fits; peaks were not resolvable for $PC_{61}BM$ contents larger than 70%.

PIPCP:$PC_{61}BM$ film incorporating 30 wt% $PC_{61}BM$ shows the highest intensity in PIPCP scattering peaks, and therefore, this blend ratio was selected for our annealing study. Fig. 5(a) and (b) display the GIWAXS pattern of the BHJ film with 30 wt% of $PC_{61}BM$ held at the annealing temperature of 200 and 225 °C. The remaining GIWAXS patterns with varying annealing temperature are provided in Fig. s5.† The GIWAXS of unannealed PIPCP:$PC_{61}BM$ film featured the backbone stacking, lamellar stacking, and π–π stacking peaks. In Fig. s5(a)–(d),† this pattern persisted with annealing to 150 °C. Further increasing the annealing temperature to 200 and 225 °C [Fig. 5(a) and (b), respectively] caused the lamellar stacking to shift to lower q values. The integrated in-plane line profiles with varying annealing temperature are shown in Fig. 5(c). The backbone scattering peak at about 0.25 $Å^{-1}$ is unaffected with increasing temperature, corresponding to a nearly constant d-spacing of 25 Å (Fig. 5(d)). This behavior is expected, since the strong bonds within the backbone result in weak thermal expansion. This observation supports our assignment of this peak to backbone periodicity.

Fig. 5(d) also displays the d-spacing of the in-plane (IP) and out-of-plane (OOP) components of lamellar stacking with varying annealing temperature. Refraction of the X-rays can slightly increase the observed q position of scattering peaks in the out-of-plane direction.[23] To account for refraction, we calculated the peak shift following the methodology in the literature,[23] and found that refraction will result in a shift of 0.007 $Å^{-1}$. Thus, we subtracted this from our results before calculating the d-spacing. When the annealing temperature is below 150 °C, the IP d-spacing is nearly constant but then slowly increases up to 225 °C. In contrast, the d-spacing of OOP lamellar stacking is smaller than for the IP and increases slightly non-linearly, with temperature. These observations suggest that the BHJ film is laterally constrained by the substrate below about 225 °C, but becomes unconstrained above this temperature. From the lamellar d-spacing in Fig. 5(d) we can estimate the linear coefficient of thermal expansion (CTE).[24] The slightly nonlinear behavior in Fig. 5(d) complicates this calculation and hence we simply estimate the CTE of lamellar stacking by a line through the OOP d-spacing data and obtain $(10 \pm 5) \times 10^{-4}\ °C^{-1}$. This is close, but somewhat larger than, the CTE of the P3HT lamella spacing ($\sim 4.8 \times 10^{-4}\ °C^{-1}$) and the CTE of the PTB7 π–π stacking ($\sim 3.5 \times 10^{-4}\ °C^{-1}$).[24,25]

The presence of a molecular mixed phase in the BHJ films has been reported in several polymer : fullerene systems. The mixed phase is observed for P3HT:$PC_{61}BM$,[7] poly(2,5-bis(3-tetradecylthiophen-2-yl)thieno[3,2-*b*]thiophene) (pBTTT):$PC_{71}BM$,[26] poly[[2,6′-4,8-di(5-ethylhexylthienyl)benzo[1,2-*b*;3,3-*b*]dithiophene]3-fluoro-2[(2-ethylhexyl)carbonyl]thieno[3,4-*b*]thiophenediyl] (PTB7-Th):$PC_{71}BM$,[27] and PBDTTPD:$PC_{61}BM$.[12] In contrast, the absence of the mixed phase is observed for poly[(5,6-difluoro-2,1,3-benzothiadiazol-4,7-diyl)-*alt*-(3,3‴-di(2-octyldodecyl)-2,2′;5′,2″;5″,2‴-quaterthiophen-5,5‴-diyl)](PffBT4T-2OD or PCE11):$PC_{61}BM$[28] which is similar to our observation, as well as for some small molecule : fullerene OSCs.[15] These results show that the mixed phase is varied in the reported systems, relying on the formation of preferable morphology that facilitates electron–hole separation. We also note that there are several methods to improve the order of polymers in BHJs such as solvent additives[29] and thermal treatment.[30,31] In the case of PIPCP, the ordering is improved by incorporating $PC_{61}BM$. We speculate that the improved crystallinity of PIPCP:$PC_{61}BM$ blends is due to the interactions between the PIPCP branched sidechains and the $PC_{61}BM$. Similar behavior was reported for a series of anthracene containing poly(*p*-arylene-ethynylene)-*alt*-poly(*p*-arylene-vinylene)s polymers, abbreviated AnE-PV. Here, the crystallinity of AnE-PVstat is enhanced after blending with $PC_{61}BM$, and was ascribed interactions of the sidechains,[32,33] consistent with recent work.[34]

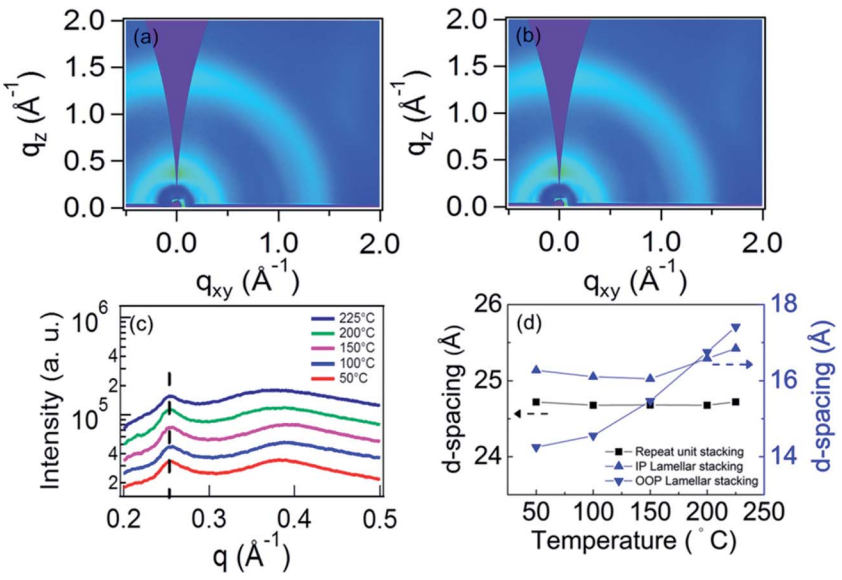

Fig. 5 The GIWAXS pattern of PIPCP:$PC_{61}BM$ BHJ film incorporating 30 wt% of $PC_{61}BM$ with holding the annealing temperature at (a) 200 and (b) 225 °C. (c) The in-plane line profiles integrated from the GIWAXS pattern with holding the annealing temperature at 50, 100, 150, 200 and 225 °C. (d) The d-spacing of lamellar and repeat unit stacking with varying the annealing temperature.

4. Conclusion

We have investigated the blend morphology of PIPCP:$PC_{61}BM$ BHJs by varying the $PC_{61}BM$ composition within the BHJ. GIWAXS shows that $PC_{61}BM$ not only prefers to aggregate in the film, resulting in no mixed phase in the BHJ, but remarkably improves the order of the PIPCP polymer along the backbone, consistent with an increased conjugation length of the polymer. This behavior is unusual since most often, blending conjugated polymers with PCBM decreases the order in the polymer. We speculate that the improved backbone order (or increased conjugation length) due to $PC_{61}BM$ incorporation into the BHJ results to the low energy loss (E_{loss}) of the OSC device.

Conflicts of interest

The authors declare no conflict of interest.

Acknowledgements

Work was supported by the Department of the Navy, Office of Naval Research Award No. N00014-14-1-0580, N00014-16-1-2520 and N00014-16-1-2678. Use of Stanford Synchrotron Radiation Lightsource, SLAC National Accelerator Laboratory, is supported by the U.S. Department of Energy, Office of Science, Office of Basic Energy Sciences, under Contract No. DE-AC02-76SF00515. Part of this work was performed at the Stanford Nano Shared Facilities (SNSF), supported by the National Science Foundation under award ECCS-1542152. Tzu-Yen Huang acknowledges the support of Ministry of Science and Technology (MOST), Taiwan though the Overseas Project for Postdoctoral Research Abroad Program (PRAP) (105-2917-I-564-044). Victoria Savikhin acknowledges the support of the Department of Defense (DoD) through the National Defense Science & Engineering Graduate Fellowship (NDSEG) program.

References

1 T. R. Andersen, H. F. Dam, M. Hosel, M. Helgesen, J. E. Carle, T. T. Larsen-Olsen, S. A. Gevorgyan, J. W. Andreasen, J. Adams, N. Li, F. Machui, G. D. Spyropoulos, T. Ameri, N. Lemaitre, M. Legros, A. Scheel, D. Gaiser, K. Kreul, S. Berny, O. R. Lozman, S. Nordman, M. Valimaki, M. Vilkman, R. R. Sondergaard, M. Jorgensen, C. J. Brabec and F. C. Krebs, *Energy Environ. Sci.*, 2014, **7**, 2925–2933.

2 M. Kaltenbrunner, M. S. White, E. D. Głowacki, T. Sekitani, T. Someya, N. S. Sariciftci and S. Bauer, *Nat. Commun.*, 2012, **3**, 770.

3 L. H. Rossander, H. F. Dam, J. E. Carle, M. Helgesen, I. Rajkovic, M. Corazza, F. C. Krebs and J. W. Andreasen, *Energy Environ. Sci.*, 2017, **10**, 2411–2419.

4 C. Lungenschmied, G. Dennler, H. Neugebauer, S. N. Sariciftci, M. Glatthaar, T. Meyer and A. Meyer, *Sol. Energy Mater. Sol. Cells*, 2007, **91**, 379–384.

5 L. Meng, Y. Zhang, X. Wan, C. Li, X. Zhang, Y. Wang, X. Ke, Z. Xiao, L. Ding, R. Xia, H.-L. Yip, Y. Cao and Y. Chen, *Science*, 2018, **361**(6407), 1094–1098.

6 H. Zhang, H. Yao, J. Hou, J. Zhu, J. Zhang, W. Li, R. Yu, B. Gao, S. Zhang and J. Hou, *Adv. Mater.*, 2018, **30**, 1800613.

7 P. Westacott, J. R. Tumbleston, S. Shoaee, S. Fearn, J. H. Bannock, J. B. Gilchrist, S. Heutz, J. deMello, M. Heeney, H. Ade, J. Durrant, D. S. McPhail and N. Stingelin, *Energy Environ. Sci.*, 2013, **6**, 2756–2764.

8 B. A. Collins, Z. Li, J. R. Tumbleston, E. Gann, C. R. McNeill and H. Ade, *Adv. Energy Mater.*, 2013, **3**, 65–74.

9 N. C. Miller, E. Cho, R. Gysel, C. Risko, V. Coropceanu, C. E. Miller, S. Sweetnam, A. Sellinger, M. Heeney, I. McCulloch, J.-L. Brédas, M. F. Toney and M. D. McGehee, *Adv. Energy Mater.*, 2012, **2**, 1208–1217.

10 B. A. Collins, J. R. Tumbleston and H. Ade, *J. Phys. Chem. Lett.*, 2011, **2**, 3135–3145.

11 W. Chen, T. Xu, F. He, W. Wang, C. Wang, J. Strzalka, Y. Liu, J. Wen, D. J. Miller, J. Chen, K. Hong, L. Yu and S. B. Darling, *Nano Lett.*, 2011, **11**, 3707–3713.

12 J. A. Bartelt, Z. M. Beiley, E. T. Hoke, W. R. Mateker, J. D. Douglas, B. A. Collins, J. R. Tumbleston, K. R. Graham, A. Amassian, H. Ade, J. M. J. Fréchet, M. F. Toney and M. D. McGehee, *Adv. Energy Mater.*, 2013, **3**, 364–374.

13 C. Zhong, J. A. Bartelt, M. D. McGehee, D. Cao, F. Huang, Y. Cao and A. J. Heeger, *J. Phys. Chem. C*, 2015, **119**, 26889–26894.

14 S. D. Oosterhout, V. Savikhin, M. A. Burgers, J. Zhang, Y. Zhang, S. R. Marder, G. C. Bazan and M. F. Toney, *J. Phys. Chem. C*, 2018, **122**, 11136–11144.

15 S. D. Oosterhout, V. Savikhin, J. Zhang, Y. Zhang, M. A. Burgers, S. R. Marder, G. C. Bazan and M. F. Toney, *Chem. Mater.*, 2017, **29**, 3062–3069.

16 M. Wang, H. Wang, T. Yokoyama, X. Liu, Y. Huang, Y. Zhang, T.-Q. Nguyen, S. Aramaki and G. C. Bazan, *J. Am. Chem. Soc.*, 2014, **136**, 12576–12579.

17 N. A. Ran, J. A. Love, M. C. Heiber, X. Jiao, M. P. Hughes, A. Karki, M. Wang, V. V. Brus, H. Wang, D. Neher, H. Ade, G. C. Bazan and T.-Q. Nguyen, *Adv. Energy Mater.*, 2018, **8**, 1701073.

18 N. A. Ran, J. A. Love, C. J. Takacs, A. Sadhanala, J. K. Beavers, S. D. Collins, Y. Huang, M. Wang, R. H. Friend, G. C. Bazan and T.-Q. Nguyen, *Adv. Mater.*, 2016, **28**, 1482–1488.

19 M. Wang, H. Wang, M. Ford, J. Yuan, C.-K. Mai, S. Fronk and G. C. Bazan, *J. Mater. Chem. A*, 2016, **4**, 15232–15239.

20 J. Yuan, M. J. Ford, W. Ma and G. C. Bazan, *J. Mater. Chem. A*, 2017, **5**, 8903–8908.

21 J. Yuan, N. A. Ran, M. J. Ford, M. Wang, M. K. Ravva, C.-K. Mai, X. Liu, J.-L. Brédas, T.-Q. Nguyen, W. Ma and G. C. Bazan, *J. Mater. Chem. A*, 2017, **5**, 18618–18626.

22 J. Ilavsky, *J. Appl. Crystallogr.*, 2012, **45**, 324–328.

23 M. F. Toney and S. Brennan, *Phys. Rev. B: Condens. Matter Mater. Phys.*, 1989, **39**, 7963–7966.

24 E. Verploegen, R. Mondal, C. J. Bettinger, S. Sok, M. F. Toney and Z. Bao, *Adv. Funct. Mater.*, 2010, **20**, 3519–3529.

25 V. Savikhin, L. K. Jagadamma, L. J. Purvis, I. Robertson, S. D. Oosterhout, C. J. Douglas, I. D. W. Samuel and M. F. Toney, *iScience*, 2018, **2**, 182–192.

26 A. C. Mayer, M. F. Toney, S. R. Scully, J. Rivnay, C. J. Brabec, M. Scharber, M. Koppe, M. Heeney, I. McCulloch and M. D. McGehee, *Adv. Funct. Mater.*, 2009, **19**, 1173–1179.
27 W. Huang, N. Chandrasekaran, S. K. K. Prasad, E. Gann, L. Thomsen, D. Kabra, J. M. Hodgkiss, Y.-B. Cheng and C. R. McNeill, *ACS Appl. Mater. Interfaces*, 2016, **8**, 29608–29618.
28 N. Li, J. D. Perea, T. Kassar, M. Richter, T. Heumueller, G. J. Matt, Y. Hou, N. S. Güldal, H. Chen, S. Chen, S. Langner, M. Berlinghof, T. Unruh and C. J. Brabec, *Nat. Commun.*, 2017, **8**, 14541.
29 G. Jing, C. Wei, D. Letian, C. Chun-Chao, C. Wei-Hsuan, L. Yongsheng, L. Gang and Y. Yang, *Adv. Mater.*, 2014, **26**, 3142–3147.
30 R. Heuvel, F. J. M. Colberts, M. M. Wienk and R. A. J. Janssen, *J. Mater. Chem. C*, 2018, **6**, 3731–3742.
31 T. Erb, U. Zhokhavets, G. Gobsch, S. Raleva, B. Stühn, P. Schilinsky, C. Waldauf and C. J. Brabec, *Adv. Funct. Mater.*, 2005, **15**, 1193–1196.
32 S. Rathgeber, J. Perlich, F. Kühnlenz, S. Türk, D. A. M. Egbe, H. Hoppe and R. Gehrke, *Polymer*, 2011, **52**, 3819–3826.
33 C. Kästner, D. A. M. Egbe and H. Hoppe, *J. Mater. Chem. A*, 2015, **3**, 395–403.
34 V. Savikhin, M. Babics, M. Neophytou, S. Liu, S. D. Oosterhout, H. Yan, X. Gu, P. M. Beaujuge and M. F. Toney, *Chem. Mater.*, 2018, **30**, 7872–7884.